

Multiwavelength spectroscopy of PSR B0656+14

Martin Durant¹, Oleg Kargaltsev¹ and George G. Pavlov^{2,3}

¹ *University of Florida, 211 Bryant Space Science Center, Gainesville, FL, USA*

² *Pennsylvania State University, 525 Davey Lab, University Park, PA, USA*

³ *St.-Petersburg State Polytechnic University, Polytekhnicheskaya ul. 29, 195251, Russia*

`martin.durant@astro.ufl.edu`

ABSTRACT

Using high-quality Hubble Space Telescope observations, we construct the near infra-red (NIR) to far ultra-violet (FUV) spectral energy distribution (SED) of PSR B0656+14. The SED is non-monotonic. Fitting it with a simple combination of a Rayleigh-Jeans spectrum (UV) and non-thermal power-law (optical/NIR) leaves significant residuals, strongly hinting at one or more spectral features. We consider various models (combination of continuum components, and absorption/emission lines) with possible interpretations, and place them in the context of the broader spectral energy distribution. Surprisingly, the extrapolation of the best-fit X-ray spectral model roughly match the NIR-FUV data, and the power-law component is also consistent with the γ -ray fluxes. We compare the multiwavelength SED of B0656+14 with those of other optical, X-ray and γ -ray detected pulsars, and notice that a simple power-law spectrum crudely accounts for most of the non-thermal emission.

Subject headings: pulsars: individual (PSR B0656+14)

1. Introduction

Pulsars are responsible for the production of high-energy emission observable across the EM spectrum from the radio to γ -rays. They are natural laboratories for investigating particle acceleration and radiation processes in the high-energy, high-field, high-gravity regime. Outside the radio, the non-thermal high energy emission is believed to be produced by incoherent processes such as synchrotron and curvature radiation. With current instrumentation, this radiation is most easily detected in γ -rays (where most of the energy is released) and X-rays (although the latter is often “contaminated” by thermal emission from the neutron star surface). It is much more challenging to detect the non-thermal emission in the optical/near-infrared (NIR).

There are few pulsars for which multicolor UV/optical/IR photometry exists (Mignani 2009; Kargaltsev & Pavlov 2007; Mignani et al. 2007). These are moderately old pulsars B1929+10 and B0950+08; $\tau \simeq 3$ Myr and 17.5 Myr, respectively),

middle-aged pulsars Geminga, B0656+14, and B1055–52 ($\simeq 300$, 100, and 500 kyr respectively), the younger Vela pulsar ($\simeq 10$ kyr), and the very young pulsars Crab (950 yrs) and B0540–69 ($\simeq 1.7$ kyr). The optical and X-ray spectra of the Vela, Crab and B0540–69, look “boring” (featureless power-laws), while the spectra of the middle-aged pulsars are more complex and exhibit both thermal (emitted from the NS surface) and non-thermal (magnetospheric) components in X-rays and optical-UV (e.g., Romani et al. 2005). No spectral feature has yet been observed in the IR-UV spectra of pulsars¹, although Zharikov et al. (2007)’s data hinted at possible feature(s) for PSR B0656+14. Here we will present detailed analysis of the IR-UV spectrum of B0656+14.

PSR B0656+14 ($P = 385$ ms; $\tau = 1.1 \times 10^5$ yr), located at the distance of 288 ± 30 pc

¹Bignami et al. (1996) claimed a feature in the optical-UV spectrum of Geminga (see also Mignani et al. 1998), but this was not supported by subsequent observations (Kargaltsev et al. 2005)

(Briskin et al. 2003), is the brightest of middle-aged pulsars, in both X-rays and optical. Its X-ray spectrum and pulse profile were studied by Anderson et al. (1993); Possenti et al. (1996); Greiveldinger et al. (1996); Marshall & Schulz (2002); Zavlin & Pavlov (2004); De Luca et al. (2005). The X-ray spectrum (0.1–6 keV), obtained from *Chandra* observations (Pavlov et al. 2002), can be fitted with a model which consists of thermal soft (TS) component with a blackbody (BB) temperature of $\simeq 0.82$ MK, emitted from a large part of the NS surface ($R \simeq 7.3$ km); thermal hard (TH) component with the BB temperature of $\simeq 1.7$ MK, apparently emitted from smaller ($R \simeq 0.5$ km) hotter areas (perhaps hot polar caps); and non-thermal power-law (PL) component, with the photon index $\Gamma \simeq 1.5$, possibly emitted from the pulsar magnetosphere. The X-ray radiation is pulsed, with a pulsed fraction of $\sim 13\%$ at lower energies (< 0.7 keV), where the TS component dominates, and $\sim 57\%$ in the 2–4 keV band, where the PL component is dominant.

The optical counterpart of PSR B0656+14 ($V \approx 25$) was discovered by Caraveo et al. (1994). Because a nearby galaxy contaminates the ground-based images (Koptsevich et al. 2001), the best near-IR/optical/near-UV ($\lambda = 0.2$ – $2 \mu\text{m}$) data were obtained with the *Hubble Space Telescope* (*HST*). The pulsar was imaged with FOC (Pavlov et al. 1996, 1997), WFPC2 (Mignani et al. 2000), and NICMOS (Koptsevich et al. 2001). These observations suggested that the pulsar has a non-thermal spectrum from NIR through the optical, with somewhat uncertain spectral index, $\alpha_\nu \simeq -0.4 \pm 0.5$ ($F_\nu \propto \nu^{\alpha_\nu}$). The large uncertainty in the slope reflects a substantial scatter among the existing photometric points. This scatter could possibly be attributed to the presence of broad spectral features or could be just the result of poor cross-calibration between different instruments that have been used to cover a broad range of wavelengths.

In addition to photometric observations, Kern et al. (2003) observed the optical pulse profile and polarization with the Palomar 5m telescope and found that the emission in 400–600 nm band is highly pulsed (upper limit on the unpulsed flux is 16%). The pulse profile is double-peaked, with a bridge of emission between the two peaks; emission from the bridge was found to be highly

polarized. Finally, the low-resolution spectrum and pulsations in the near-UV (NUV) have been measured with *HST* STIS (Shibanov et al. 2005). They found that NUV pulse profile is also double-peaked and similar to the optical one. The high pulsed fraction, $70 \pm 12 \%$, and a flat spectrum ($\alpha_{\nu, \text{NUV}} = 0.35 \pm 0.5$) suggest that NUV emission is mostly non-thermal. Since the soft X-ray spectrum is thermal and optical spectrum is non-thermal, a transition between the thermal and non-thermal spectra is expected to occur somewhere in between. Kargaltsev & Pavlov (2007) show that the FUV flux is consistent with a low pulsed fraction thermal component and a highly pulsed non-thermal component.

To better constrain the shape of the spectrum and evaluate contributions of the thermal and non-thermal components, we observed B0656 using instruments aboard *HST* (ACS, STIS and COS). Together with re-analysis of archival NICMOS observations, we present the most complete infrared to ultraviolet spectral energy distribution measured for any pulsar. The data analysis of the observations, including the archival ones, is described in Section 2 and Appendix A. In Section 3, we present the results, both the photometry and spectra from the individual observations, and the combined spectral energy distribution. In Section 4 we discuss the interpretation of the measured spectral shape, its context in the wider spectral energy distribution, and comparisons with the spectra of other pulsars.

2. Observations and analysis

In Table 1 we list the observations analyzed as part of this work. Of these, the NICMOS and STIS NUV/FUV observations were reported before (Koptsevich et al. 2001; Shibanov et al. 2005; Kargaltsev & Pavlov 2007), but we reanalyze the data from the archive with the latest calibration applied. The rest of the data appear here for the first time.

Table 2 summarizes previously published optical/UV observations of B0656+14, which we will not re-analyze in this paper. We will include the results of these observations with those produced in this work, for comparison.

Below, we briefly describe the fluxes and spectra derived for each data-set, in order of increasing

TABLE 1
LOG OF HST OBSERVATIONS FOR ANALYSIS

Date	Program ID	Instrument/ optical element	Wavelength (Å)	Exposure time (s)
1998-03-18	7836	NICMOS/F110W	11285	2544
	7836	NICMOS/F160W	16056	5089
	7836	NICMOS/F187W	18718	7633
2001-09-01	9156	STIS/prism	1750–3000	6791
2001-11-16	9156	STIS/prism	1750–3000	12761
2004-01-20	9797	STIS/G140L	1150–1700	4950
2005-12-03	10600	ACS/FR647M	6820	810
	10600	ACS/FR647M	7393	810
	10600	ACS/FR914M	7956	747
	10600	ACS/FR914M	8751	1331
2005-12-08	10600	ACS/FR914M	9491	2842
	10600	ACS/FR459M	4029	1400
	10600	ACS/FR459M	4401	1020
	10600	ACS/FR459M	4780	830
	10600	ACS/FR459M	5165	885
	10600	ACS/FR647M	5566	1020
	10600	ACS/FR647M	6244	1020
2010-02-17	11629	COS/G140L	1100–1700	10927
2010-02-20	11629	COS/G140L	1100–1700	10927

NOTE.—Wavelengths are either the sensitive range of a spectroscopic observation, or the pivot wavelength of a photometric observation.

Table 2: List of previously published observations and results.

Instrument	Filter	Central Frequency (10^{14} Hz)	Flux F_ν (μ Jy)	Reference
HST/WFPC2	F555W	5.48	0.39(2)	1
HST/FOC	F555W	5.62	0.39(2)	2
HST/FOC	F430W	7.28	0.26(3)	3
HST/FOC	F342W	8.81	0.31(3)	3
HST/FOC	F195W	12.7	0.35(4)	3
BTA/CCD	I	3.80	0.60(6) ^a	4
BTA/CCD	R	4.61	0.39(3)	4
BTA/CCD	V	5.46	0.37(4)	4
BTA/CCD	B	6.84	0.32(4)	4
Subaru/Suprime	I	3.80	0.37(4)	5
Subaru/Suprime	R	4.61	0.42(3)	5
Subaru/Suprime	B	6.84	0.31(2)	5
VLT/FORS2	4300–9600 Å			6

Note: references (1) Mignani et al. (1997) (2) Pavlov et al. (1996) (3) Pavlov et al. (1997) (4) Koptsevich et al. (2001) (5) Shibanov et al. (2006) (6) Zharikov et al. (2007). Numbers in parentheses indicate the uncertainty in the final digit.

^a: The authors note that this measurement was contaminated by a nearby red galaxy.

wavelength. Full details of the data reduction procedures used are given in the Appendix. We encourage interested readers to refer to the Appendix for a thorough account of the specific procedures required for the analysis of the diverse data, in particular grating spectroscopy (with a slit), slit-less prism spectroscopy, very faint infrared photometry (requiring custom NICMOS darks), ramp filter photometry and the evaluation of calibration performance in the IR-optical regime.

2.1. STIS FUV grating

The measured flux values are given in Table 3, while the spectrum is shown in Figure 1. The total flux in the 1153–1700 Å range ($\Delta\lambda = 547$ Å), can be estimated as $F \simeq \Delta\lambda (\sum_i \langle F_\lambda \rangle_i \Delta\lambda_i) (\sum_i \Delta\lambda_i)^{-1} \simeq (4.28 \pm 0.28) \times 10^{-15} \text{ erg s}^{-1} \text{ cm}^{-2}$, corresponding to the luminosity $L_{\text{FUV}} = 4\pi d^2 F = (4.24 \pm 0.28) \times 10^{28} d_{288}^2 \text{ erg s}^{-1}$.

For a typical NS radius $R = 13$ km and distance $d = 288$ pc, the inferred brightness temperatures are 0.615 ± 0.026 , 0.663 ± 0.028 , 0.715 ± 0.031 , and 0.832 ± 0.036 MK, for $E(B - V) = 0.01$, 0.02 , 0.03 , and 0.05 , respectively; the corresponding χ_ν^2 values are 0.663 , 0.642 , 0.626 , and 0.611 , for 4 degrees of freedom (dof). An example of best-fit blackbody spectrum is shown in Figure 1, for a plausible $E(B - V) = 0.02$. The corresponding unabsorbed bolometric luminosity can be estimated as $L_{\text{bol}} = 1.2 \times 10^{29} T_5^4 R_{13}^2 \text{ erg s}^{-1}$; for instance, $L_{\text{bol}} = (2.3 \pm 0.4) \times 10^{32} \text{ erg s}^{-1}$ for $E(B - V) = 0.02$, $R = 13$ km and $d = 288$ pc.

2.2. COS spectroscopy

The measured spectrum is shown in Figure 2 while the spectral fluxes are listed in Table 4. An absorbed PL, $F_\lambda \propto \lambda^{-\alpha_\lambda}$, with best-fit $\alpha_\lambda = 3.0 \pm 0.2$ is plotted. The curve follows the overall shape of the spectrum well, but there is substantial scatter resulting in $\chi_\nu^2 = 2.1$. The majority of this scatter is in a few outlier points which not appear to form spectral feature(s). We cannot rule out narrow lines, but such lines are not expected for the high temperature and pressure of a NS atmosphere or magnetosphere. We find no obvious reason for the additional scatter, and speculate that it may be due to the imperfections of the calibration or structure in the detector back-

ground.

2.3. STIS NUV prism

The measured flux values are given in Table 5, while the spectrum is shown in Figure 3. The total flux in the 1790–2950 Å range ($\Delta\lambda = 1160$ Å), can be estimated as $(2.63 \pm 0.38) \times 10^{-15} \text{ erg s}^{-1} \text{ cm}^{-2}$, corresponding to the luminosity $L_{\text{NUV}} = 4\pi d^2 F = (2.61 \pm 0.38) \times 10^{28} d_{288}^2 \text{ erg s}^{-1}$. The obtained average flux is slightly larger, but compatible with the flux measured by Shibano et al. (2005) in somewhat wider wavelength interval (1700 – 3400 Å).

We then fit the NUV spectrum with the absorbed power-law model, $F_\lambda = F_{2500} (\lambda/2500 \text{ Å})^{\alpha_\lambda} \times 10^{-0.4A(\lambda)E(B-V)}$. For plausible values $E(B - V) = 0.01$, 0.02 , 0.03 and 0.05 , we find the power-law indices $\alpha_\lambda = -2.92 \pm 0.41$, -3.01 ± 0.41 , -3.09 ± 0.41 and -3.24 ± 0.41 , and the normalization $F_{2500} = 1.85 \pm 0.08$, 1.97 ± 0.09 , 2.11 ± 0.10 and $2.41 \pm 0.11 \times 10^{-18} \text{ erg cm}^{-2} \text{ s}^{-1} \text{ Å}^{-1}$, respectively; the corresponding χ_ν^2 values are 1.27 , 1.38 , 1.51 , and 1.87 , for 5 dof. The obtained spectral slopes are systematically smaller than those derived from our fits to the FUV spectrum. The flattening of the spectrum at longer wavelengths can be attributed to a larger relative contribution of the non-thermal component. The measured slope of the NUV spectrum for $E(B - V) = 0.03$, $\alpha_\nu \simeq 1.1 \pm 0.4$ ($\alpha_\nu = -\alpha_\lambda - 2$), is marginally compatible with the slope $\alpha_\nu = 0.35 \pm 0.5$ found by Shibano et al. (2005). The difference can be attributed to the different choice of the spectral bins and narrower wavelength range that we used.

2.4. ACS/WFC Ramp Filter Photometry

The photometric fluxes for three ramp filters and a total of 11 central wavelength positions are listed in Table 6 and shown in Figure 4. Given the non-standard nature of the ramp filter photometry, we performed a specific check on our calibration in Section A.6. We find the pipeline calibration satisfactory.

2.5. NICMOS photometry

We find $F_\nu(\text{F110W}) = 0.385 \pm 0.030 \mu\text{Jy}$; $F_\nu(\text{F160W}) = 0.551 \pm 0.030 \mu\text{Jy}$; $F_\nu(\text{F187W}) = 0.660 \pm 0.025 \mu\text{Jy}$ (uncertainties are $1-\sigma$ and statistical only). Due to the non-standard processing

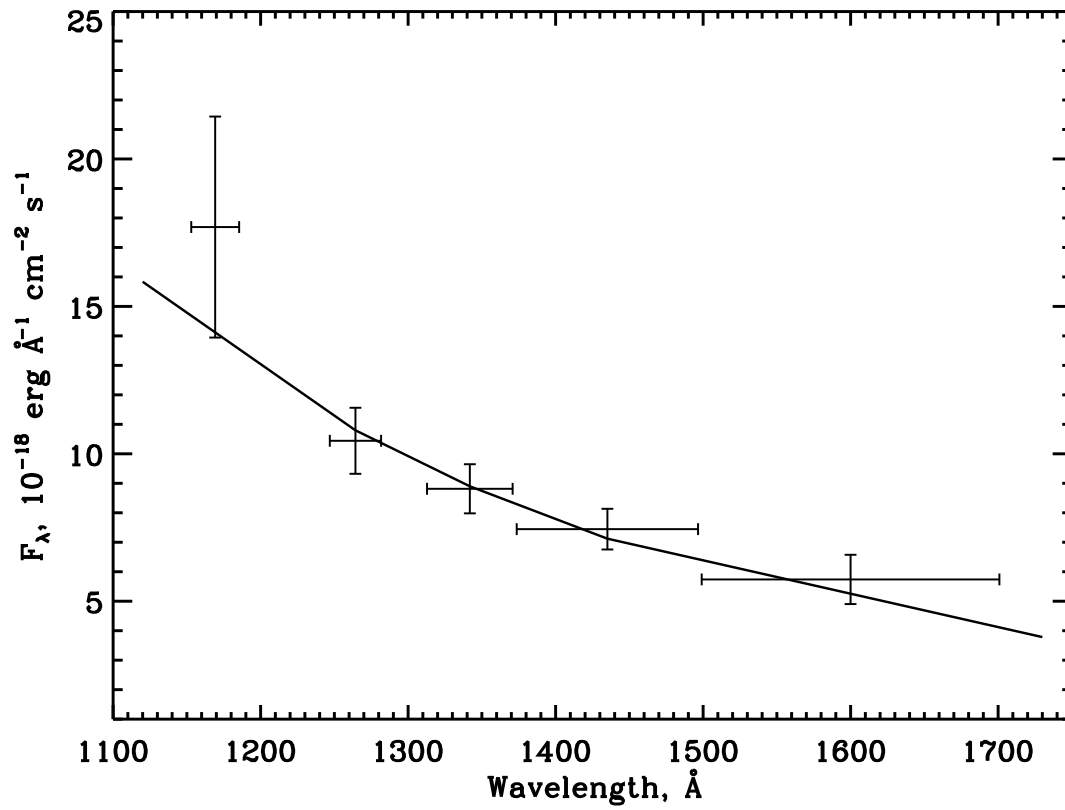


Fig. 1.— STIS FUV spectrum of B0656. The solid line shows an absorbed black-body spectrum with $T = 0.663 \text{ MK}$ and $E(B - V) = 0.02$.

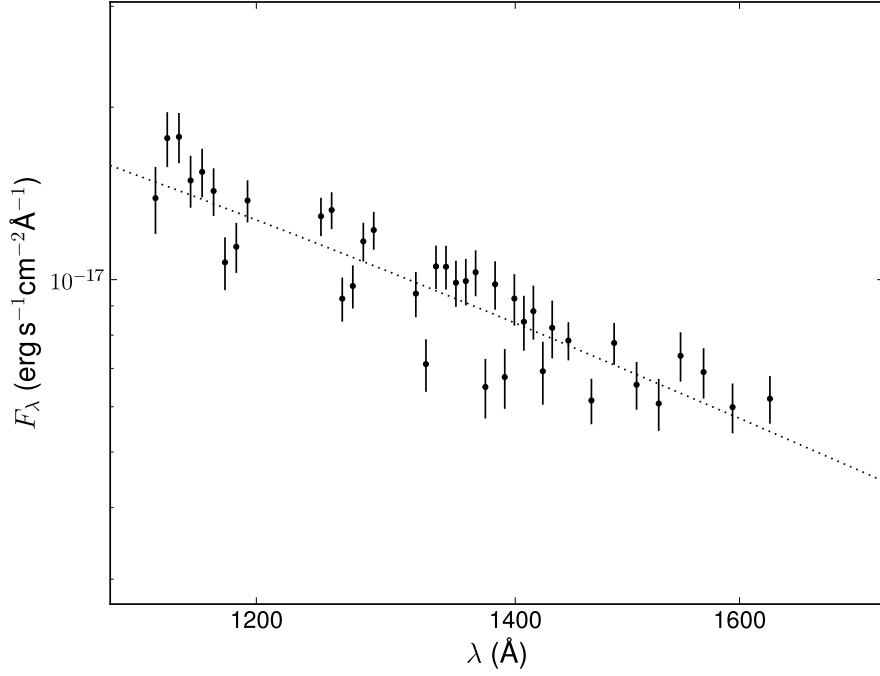


Fig. 2.— COS-FUV spectrum of PSR B0656+14. The gaps are due to the discarded data strongly affected by geocoronal emission lines (see Section 2.2). An absorbed PL fit is plotted, with $F_\lambda = \lambda^{-\alpha_\lambda} \times 10^{-0.4A(\lambda)E(B-V)}$, $\alpha_\lambda = 3.0 \pm 0.2$, $E(B-V) = 0.03$.

steps and calibration involved, we conservatively estimate the systematic uncertainty to be about 10% in each case (see Section A.6). Our flux values are only marginally consistent with those reported by Koptsevich et al. (2001). We believe that by using the most up-to-date calibration, our values should be the most accurate. We verify our calibration in Section A.6.

3. Results and discussion

3.1. IR-FUV spectrum

The final spectrum shown in Figure 4 includes both the fluxes/spectra calculated in this work and those from the literature (see Table 2). This is, to our knowledge, the most complete IR-UV spectrum of a non-recycled pulsar.

3.1.1. Qualitative spectral shape

Clearly, the spectrum of B0656 shown in Figure 4 does not fit to a simple absorbed PL model. The spectrum appears to be more complex, with some structure. Therefore we begin by making some qualitative statements.

The upturn of the spectrum in the NUV range is consistent with a contribution by a thermal, Rayleigh-Jeans (R-J; $F_\nu \propto \nu^2$) component that is most prominent in FUV and also consistent with the extrapolation of the X-ray TS component to the optical (see also Kargaltsev & Pavlov 2007). However, even with the thermal component added, any simple PL fit to the optical spectrum of B0656 leaves large residuals. In particular, there is a deep minimum in the spectral flux around $\nu = 3 \times 10^{14}$ Hz ($\lambda = 1 \mu\text{m}$), with steep rises to either side (see Figure 4).

The complex spectral shape can be interpreted in several ways. For instance, the steep rise at the lowest frequencies could be attributed to a cool, $T \sim 1000$ K, thermal (disk) component. Alternatively, the spectrum is very suggestive of *spectral features*, either two absorption lines or a very broad emission line. We have fitted models corresponding to these three scenarios with the best-fit parameters listed in Table 7. The corresponding models and residuals are shown in Figure 5. We note that none of the fits is statistically good ($\chi_\nu^2 > 1.5$), but these fits do not show systematic structure in the residuals. Of the three,

the absorption model, with lines at (2.91 ± 0.03) and $(8.05 \pm 0.09) \times 10^{14}$ Hz ($\lambda = 1.030 \pm 0.011$ and $0.372 \pm 0.004 \mu\text{m}$), is statistically preferred.

3.1.2. Possible interpretations

Several possible interpretations for spectral features can be considered. As an example, we illustrate the apparently straightforward case of *cyclotron* emission (or absorption). Given the current uncertainties of the optical flux, we could speculate that we are observing cyclotron lines from a cool plasma. The NS magnetosphere has a dipole magnetic field $B \propto (R_{NS}/r)^3$ with surface strength $B_{\text{dipole}} \sim 5 \times 10^{12}$ G. An electron cyclotron line centred at $\lambda \approx 1 \mu\text{m}$ would require magnetic field $B \sim 2 \times 10^8$ G, which would place the line forming region at $d \approx 300 R_{NS}$ from the NS surface but still well within the light cylinder radius ($R_{LC} = 1.15 \times 10^5 R_{NS}$).

A deep dip at $1 \mu\text{m}$ ($\nu = 3 \times 10^{14}$ Hz; Figure 4) could signify a strong absorption line, and so suggest the hypothesis of an absorbing cyclotron-resonance layer which could be composed of e^+/e^- (Rajagopal & Romani 1997; Wang et al. 1998; Ruderman 2003). Such a layer can significantly reprocess/change thermal radiation from the hot NS surface. If confirmed by more sensitive observations of B0656, quantitative measurements (centroid, line width, phase dependence) will open a new window to probe the structure of the pulsar magnetosphere.

Alternatively, there may be a *cold thermal* component in the infra-red (a steepening rise towards the red) which could be indicative of a passive post-supernova fall-back disk (Chevalier 1989) for which we estimate a temperature of about 500-1500 K. This would suggest a link to magnetars, where such fall-back disks have already been suggested (Wang et al. 2006), and support recent models that predict the persistence of fall-back disks to much later epochs than recently thought (D’Angelo & Spruit 2011).

3.2. Broad-band multi-wavelength spectrum

Let us consider the NIR-UV spectrum of B0656 in a broader, multi-wavelength context. B0656 has been extensively studied in X-rays (e.g., Pavlov et al. 2002; De Luca et al. 2005), and has

also been detected as a γ -ray source by *Fermi* LAT with high significance (Abdo et al. 2010b).

We downloaded *Chandra* ObsID 2800 (25 ks exposure with ACIS in continuous clocking [CC] mode; see also Pavlov et al. 2002) and also the spectrum of ObsID 130 (38 ks exposure with the HRC and low-energy transmission grating [LETG]; see Marshall & Schulz 2002). The data were reduced using standard procedures. We convert the counts spectra to fluxes by dividing the count rate in each bin by the calibrated effective area in that bin (sometimes called ARF), after convolving with the response function (sometimes called RMF). Although such ‘fluxing’ can produce an incorrect spectral shape at sharp detector sensitivity edges and spectral features², the deviations are confined to relatively narrow energy ranges, and the spectrum obtained in this way is independent of any pre-supposed spectral model. We also used the fluxes from the second *Fermi* catalog (2FGL; The Fermi-LAT Collaboration 2011).

In Figure 6 we show these data along with the NIR-UV fluxes. Note, however, that the extinction (and optical/UV reddening) is rather uncertain, and has a particularly strong effect at the softest X-ray energies ($E \sim 100$ eV).

We have plotted in Figure 6 the best-fit X-ray model from Pavlov et al. (2002), fitted to the same *Chandra* data³. The extrapolation of the X-ray model, the sum of two black-bodies and a power-law, is shown in the inset of Figure 6. Surprisingly, both components fall close to the UV-optical spectrum (Section 3.1). Extrapolating the X-ray fits into the NIR-UV exacerbates the uncertainties in the model flux: a small uncertainty in any given parameter translates into a large uncertainty in the predicted flux in the NIR-UV regime. It is natural to assume that the Rayleigh-Jeans spectral component is a continuation of the cooler X-ray

black-body; for a temperature of $T = 0.82$ MK, its radius would be $R \approx 10$ km (as observed at infinity) to fit the FUV, with a 15% uncertainty on T for the reddening range $0.01 < E(B - V) < 0.05$. The power-law component in the optical could, in principle, be a continuation of non-thermal power-law emission seen in X-rays (but would not be sufficient to describe the data without the features or a cool disk; see Section 3.1.1).

The extrapolation of the best-fit PL also happens to fall close to the *Fermi* γ -rays fluxes, hinting that a single very broad PL with photon index $\Gamma_{\text{MW}} = 1.50 \pm 0.05$ could in principle describe the entire non-thermal spectrum from optical to γ -rays. In order to match the GeV fluxes, the PL should of course be modified by a high-energy cut-off, normally seen for γ -ray pulsars (Abdo et al. 2010b). The high pulsed fraction ($>50\%$) in the *Fermi* LAT light-curve (Abdo et al. 2010b) and also in the optical (Kern et al. 2003) confirms that both are magnetospheric.

3.3. Comparison to other pulsars

Less than 1% of radio pulsars have been detected in the NIR-optical-UV spectral window to date. Of those all have been detected in X-rays but only some in γ -rays (Table 8). We note that this sample includes members that are young and energetic, middle-age pulsars such as B0656+14, and one millisecond (recycled) pulsar (MSPs). No isolated (i.e., non-accreting) pulsar has yet been discovered in the IR-UV range without having previously been detected in the radio and X-rays.

We retrieved the IR/optical/UV fluxes and X-ray spectra of the pulsars in Table 8, using our previous work (e.g., Durant et al., 2011; Pavlov et al. 2001; Zavlin & Pavlov 2004), X-ray spectral products downloaded from the Xassist project⁴, or, for the case of B1951+32, by re-processing data from the archives. Note that the low-significance optical detection of B1951+32 (Butler et al. 2002; Moon et al. 2004) has not been confirmed. The GeV fluxes were taken from the 2FGL catalog (The Fermi-LAT Collaboration 2011).

In Figure 7 we show the IR-GeV spectra of the pulsars in Table 8, except for the Crab (see Kuiper et al. 2001). Figure 8 shows the same

²X-ray detectors are prone to ‘redistribution’, the possibility that a photon produces a signal corresponding to a different energy.

³De Luca et al. (2005) fitted the same model to *XMM-Newton* data, and found fit parameters formally inconsistent with the ones obtained from the *Chandra* data; whereas (Zavlin & Pavlov 2004) found consistent parameters. We note that even within the *XMM-Newton* data there are obvious discrepancies between the spectra from two different instrument modes for $E < 0.5$ keV (see Figure 2 from De Luca et al. 2005) and therefore the best-fit uncertainties have likely been underestimated.

⁴<http://xassist.pha.jhu.edu/zope/xassist>

data, but in terms of ‘spectral efficiency’, $\eta_\nu \equiv 4\pi d^2 \nu F_\nu / \dot{E}$. We have sketched PL lines which connect the γ -ray fluxes with the optical for each spectrum and find that in each case the line also passes through the high-energy, non-thermal part of the X-ray spectrum. This suggests that each pulsar’s non-thermal spectrum can be empirically described by a single PL stretching across many orders of magnitude in frequency, with a break or cut-off at GeV energies. Note, that Abdo et al. (2010a) have already considered whether the γ -ray and X-ray non-thermal spectra may be consistent, and conclude that they are not (see their Figure 5); however, there is no discussion there of the uncertainties in the fitted parameters or of the effect of the choice of model function (e.g., atmosphere models for X-rays and broken power-laws in γ -rays). In Table 8 we give the appropriate spectral indices of the lines we have sketched (these are not true fits to the data). The range of the photon index, $1.2 \leq \Gamma_{\text{MW}} \leq 1.65$, is remarkably narrow. We note that the scales in the Figure are logarithmic, and there may well be additional structure on top of the speculative underlying PL component (as detected in B0656, see Figure 6), but surprisingly it appears that a remarkably simple description can be applied for a number of pulsars. We note that such a simple description is not universal, as it is not appropriate for very young pulsars such as the Crab⁵.

Recently Danilenko et al. (2011) presented evidence for steeply-rising infra-red excesses in the Geminga and Vela pulsars (the former only a marginal detection). It may be that this is a common feature of middle-aged pulsars. For Geminga, which has a similar spectrum, luminosity and distance to PSR B0656+14, they conclude that the IR excess (if it is real) can be successfully modeled with a cool irradiated disk truncated at an inner radius comparable to the light cylinder $R_{LC} = 0.016 R_\odot$. In the case of PSR B0656+14, we do not have good enough data to attempt to model disk-like emission, and *Spitzer* observations cannot resolve the pulsar from the brighter nearby galaxy. Ground-based adaptive optics in the 2-4 μm range and/or better signal-to-noise in the current infra-

red range (using the newer Wide Field Camera 3 on *HST*) should clarify the situation.

4. Summary

The IR-UV spectrum of PSR B0656+14 is non-monotonic, and requires a combination of emission or absorption lines and/or continuum components. The putative features might be explained as cyclotron lines, hinting at an outer-magnetospheric electron belt. There is also the possibility of a cold ($T \sim 1000\text{ K}$) thermal component, such as a passive, dusty circumstellar disk. Further observations in the IR are required to confirm and probe the potential disk component.

The multi-wavelength spectrum of PSR B0656+14 suggests that a single, very broad PL component can describe the non-thermal emission surprisingly well. Interestingly, there may be evidence for such a component in other pulsars that have both γ -ray and IR/optical data. A survey of γ -ray pulsars in the IR can shed light on the ubiquity of the ultra-broad power-law magnetospheric component.

Acknowledgements Based on *HST* programs GO-7836, GO-9156, GO-9797, GO-10600 and GO-11629). Support was provided by NASA through grants from the Space Telescope Science Institute, which is operated by the Association of Universities for Research in Astronomy, Inc., under NASA contract NAS5-26555. We also made use of archival *Chandra* observations provided by the HEASARC service. This work was partially supported by NASA grant NNX09AC84G and by the Ministry of Education and Science of the Russian Federation (contract 11.G34.310001). We are indebted to S. Zharikov for providing the VLT spectrum. We also thank D. Thatte of STScI for providing the dark frame required for the NICMOS reduction.

REFERENCES

- Abdo, A. A., et al. 2010a, *ApJ*, 712, 1209
- . 2010b, *ApJS*, 187, 460
- Anderson, S. B., Cordova, F. A., Pavlov, G. G., Robinson, C. R., & Thompson, Jr., R. J. 1993, *ApJ*, 414, 867
- Bignami, G. F., Caraveo, P. A., Mignani, R., Edelstein, J., & Bowyer, S. 1996, *ApJ*, 456, L111+

⁵The recent high-energy spectrum of the Crab is shown in the recent poster confluence.slac.stanford.edu/download/attachments/102860834/KUIPER_PSR_S2.N19.POSTER.pdf

- Briskin, W. F., Thorsett, S. E., Golden, A., & Goss, W. M. 2003, *ApJ*, 593, L89
- Butler, R. F., Golden, A., & Shearer, A. 2002, *A&A*, 395, 845
- Caraveo, P. A., Bignami, G. F., & Mereghetti, S. 1994, *ApJ*, 422, L87
- Chevalier, R. A. 1989, *ApJ*, 346, 847
- Chiaberge, M., Lim, P. L., Kozhurina-Platais, V., Sirianni, M., & Mack, J. 2009, Updated CTE photometric correction for WFC and HRC, Tech. rep.
- D’Angelo, C. R., & Spruit, H. C. 2011, *MNRAS*, 416, 893
- Danilenko, A. A., Zyuzin, D. A., Shibarov, Y. A., & Zharikov, S. V. 2011, *MNRAS*, 415, 867
- De Luca, A., Caraveo, P. A., Mereghetti, S., Negroni, M., & Bignami, G. F. 2005, *ApJ*, 623, 1051
- Greiveldinger, C., et al. 1996, *ApJ*, 465, L35+
- Kargaltsev, O., & Pavlov, G. 2007, *Ap&SS*, 308, 287
- Kargaltsev, O., Pavlov, G. G., & Romani, R. W. 2004, *ApJ*, 602, 327
- Kargaltsev, O. Y., Pavlov, G. G., Zavlin, V. E., & Romani, R. W. 2005, *ApJ*, 625, 307
- Kern, B., Martin, C., Mazin, B., & Halpern, J. P. 2003, *ApJ*, 597, 1049
- Koptsevich, A. B., Pavlov, G. G., Zharikov, S. V., Sokolov, V. V., Shibarov, Y. A., & Kurt, V. G. 2001, *A&A*, 370, 1004
- Kuiper, L., Hermsen, W., Cusumano, G., Diehl, R., Schönfelder, V., Strong, A., Bennett, K., & McConnell, M. L. 2001, *A&A*, 378, 918
- Landsman, W., Bohlin, R. C., Neff, S. G., O’Connell, R. W., Roberts, M. S., Smith, A. M., & Stecher, T. P. 1998, *AJ*, 116, 789
- Marshall, H. L., & Schulz, N. S. 2002, *ApJ*, 574, 377
- Mignani, R., Caraveo, P. A., & Bignami, G. F. 1997, *The Messenger*, 87, 43
- Mignani, R. P. 2009, ArXiv e-prints, 0908.1010
- Mignani, R. P., Caraveo, P. A., & Bignami, G. F. 1998, *A&A*, 332, L37
- Mignani, R. P., De Luca, A., & Caraveo, P. A. 2000, *ApJ*, 543, 318
- Mignani, R. P., Zharikov, S., & Caraveo, P. A. 2007, *A&A*, 473, 891
- Moon, D.-S., et al. 2004, *ApJ*, 610, L33
- Pavlov, G. G., Stringfellow, G. S., & Cordova, F. A. 1996, *ApJ*, 467, 370
- Pavlov, G. G., Welty, A. D., & Cordova, F. A. 1997, *ApJ*, 489, L75+
- Pavlov, G. G., Zavlin, V. E., & Sanwal, D. 2002, in *Neutron Stars, Pulsars, and Supernova Remnants*, ed. W. Becker, H. Lesch, & J. Trümper, 273–+
- Pavlov, G. G., Zavlin, V. E., Sanwal, D., Burwitz, V., & Garmire, G. P. 2001, *ApJ*, 552, L129
- Possenti, A., Mereghetti, S., & Colpi, M. 1996, *A&A*, 313, 565
- Rajagopal, M., & Romani, R. W. 1997, *ApJ*, 491, 296
- Romani, R. W., Kargaltsev, O., & Pavlov, G. G. 2005, *ApJ*, 627, 383
- Ruderman, M. 2003, ArXiv Astrophysics e-prints, 10777
- Shibarov, Y. A., Sollerman, J., Lundqvist, P., Gull, T., & Lindler, D. 2005, *A&A*, 440, 693
- Shibarov, Y. A., et al. 2006, *A&A*, 448, 313
- The Fermi-LAT Collaboration. 2011, ArXiv e-prints
- Wang, F., Ruderman, M., Halpern, J. P., & Zhu, T. 1998, *ApJ*, 498, 373
- Wang, Z., Chakrabarty, D., & Kaplan, D. L. 2006, *Nature*, 440, 772
- Zavlin, V. E., & Pavlov, G. G. 2004, *Mem. Soc. Astron. Italiana*, 75, 458
- Zharikov, S., Mennickent, R. E., Shibarov, Y., & Komarova, V. 2007, *Ap&SS*, 308, 545

Table 3: 0656 FUV-MAMA total counts and fluxes in λ -bins

λ -bin (\AA)	Counts	Background	f_λ (10^{-19} erg/s/cm ² / \AA)
1153–1185	48	14	177(37)
1247–1282	142	33	104(11)
1313–1371	190	41	88(8)
1372–1497	223	46	74(7)
1498–1700	114	25	57(8)

TABLE 4
COS FUV TOTAL COUNTS AND FLUXES OF B0656

λ (\AA)	$\delta\lambda$ (\AA)	Counts	Background	f_λ (10^{-19} erg/s/cm ² / \AA)
1130.1	8.0	170	70	138.8 \pm 18.5
1138.0	8.0	228	87	176.6 \pm 19.4
1146.0	8.0	231	74	177.5 \pm 17.9
1153.9	8.0	214	69	149.0 \pm 15.5
1161.9	8.0	244	81	154.2 \pm 15.0
1169.8	8.0	234	70	142.8 \pm 13.6
1177.8	8.0	189	57	107.2 \pm 11.3
1185.8	8.0	223	73	114.2 \pm 11.4
1193.7	8.0	241	51	137.5 \pm 11.6
1247.1	8.0	273	55	129.0 \pm 9.9
1255.0	8.0	274	45	132.3 \pm 9.8
1263.0	8.0	203	39	92.7 \pm 8.2
1270.9	8.0	222	48	97.5 \pm 8.4
1278.9	8.0	251	43	116.6 \pm 9.1
1286.9	8.0	260	44	122.0 \pm 9.3
1319.5	8.0	195	39	94.6 \pm 8.5
1327.5	8.0	144	29	71.2 \pm 7.5
1335.5	8.0	205	39	105.5 \pm 9.2
1343.4	8.0	198	36	105.3 \pm 9.3
1351.4	8.0	187	38	98.8 \pm 9.1
1359.4	8.0	184	38	99.4 \pm 9.3
1367.4	8.0	182	34	103.0 \pm 9.5
1375.3	8.0	120	28	65.0 \pm 7.7
1383.3	8.0	171	36	98.2 \pm 9.5
1391.3	8.0	121	30	67.6 \pm 8.1
1399.2	8.0	161	39	92.7 \pm 9.6
1407.2	8.0	147	38	84.4 \pm 9.3
1415.2	8.0	146	35	88.1 \pm 9.5
1423.2	8.0	121	36	69.2 \pm 8.7
1431.1	8.0	136	37	82.4 \pm 9.5
1445.0	19.9	308	83	78.3 \pm 6.0
1464.9	19.9	249	83	61.5 \pm 5.6
1484.9	19.9	286	92	77.5 \pm 6.5
1504.9	20.0	236	84	65.6 \pm 6.3
1524.8	20.0	210	80	60.8 \pm 6.3
1544.8	20.0	234	89	73.6 \pm 7.3
1566.1	22.8	232	91	69.0 \pm 6.9
1593.4	32.0	293	141	59.9 \pm 6.0
1629.2	40.0	343	173	62.0 \pm 5.9

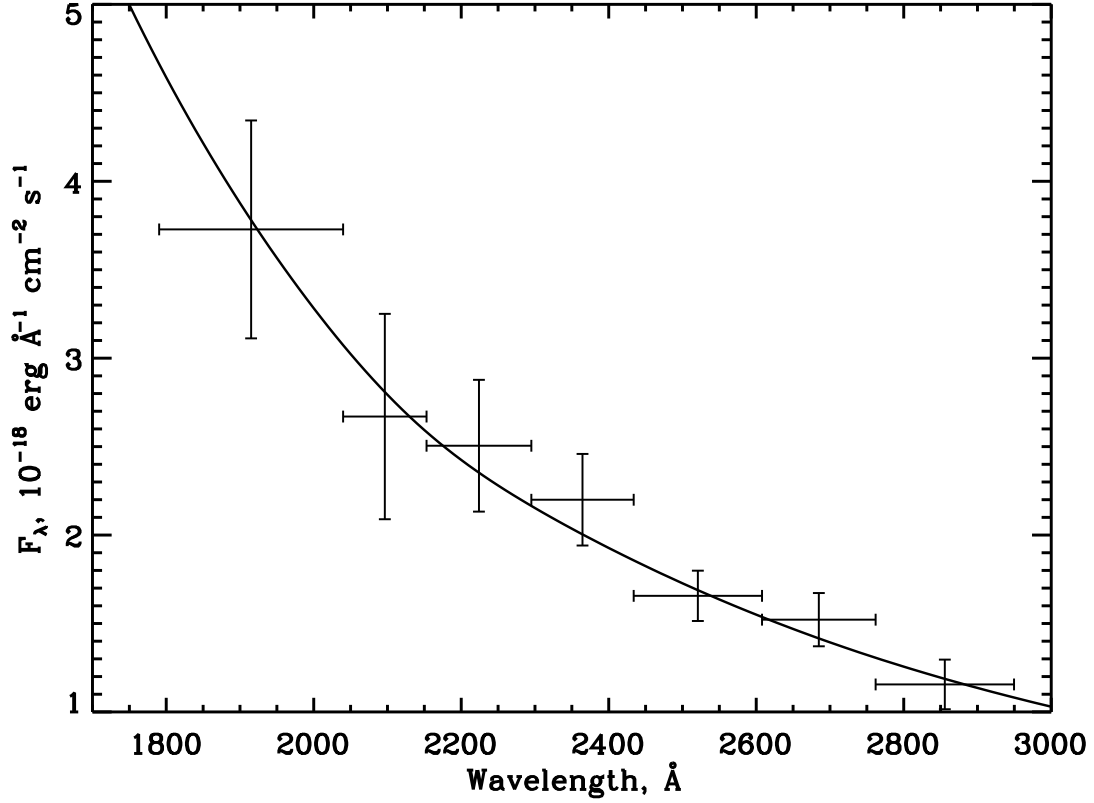


Fig. 3.— The measured (absorbed) NUV-MAMA spectrum of B0656. The curve shows the best-fit absorbed PL model with $\alpha_\lambda = -3.01$ for $E(B - V) = 0.02$.

Table 5: B0656 NUV-MAMA total counts and fluxes in nine λ -bins (+4 pixels shift in the dispersion direction is applied)

λ -bin (Å)	Counts	Background	f_λ (10^{-19} erg/s/cm ² /Å)
1790–2040	2594	2316	37(6)
2040–2153	1781	1606	27(6)
2153–2295	1889	1634	25(4)
2295–2434	1514	1251	22(3)
2434–2608	1590	1274	16.5(14)
2608–2762	1173	909	15.2(15)
2762–2950	1136	913	11.6(14)

TABLE 6
ACS/WFC RAMP FILTER FLUXES OF B0656

λ (Å)	f_ν (μJy)
4049	0.31 ± 0.3
4401	0.46 ± 0.3
4780	0.38 ± 0.3
5165	0.35 ± 0.2
5566	0.45 ± 0.3
6244	0.39 ± 0.3
6822	0.49 ± 0.2
7393	0.40 ± 0.3
7956	0.48 ± 0.3
8751	0.46 ± 0.3
9491	0.35 ± 0.5

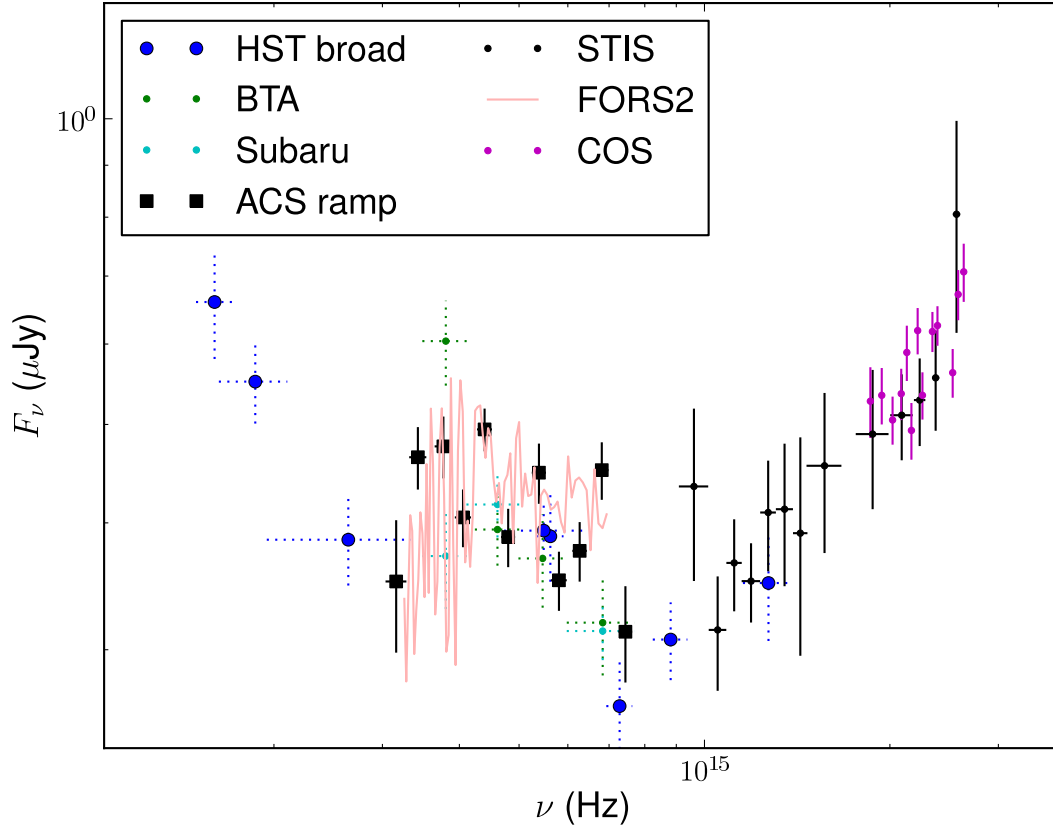


Fig. 4.— Spectrum of PSR B0656+14 (as observed). The data plotted are a combination of fluxes in the literature (Table 2) and our own work (Table 1).

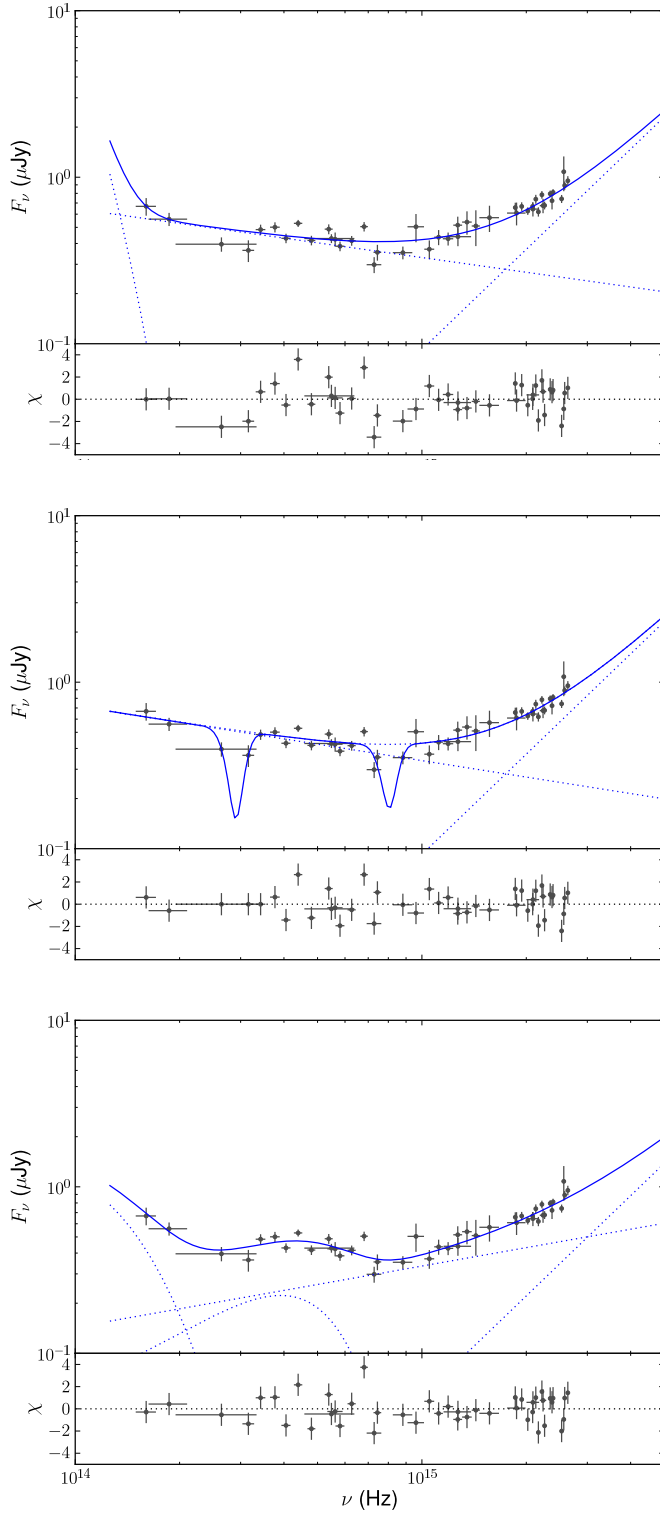


Fig. 5.— Spectral fits to the IR-UV spectrum of PSR B0656+14: continuum-only model (top), absorption lines (middle) or broad emission line (bottom) components.

TABLE 7
SIMPLE FITS TO THE IR-UV SPECTRUM

Model	T_{cold} (K)	α_ν	N_{PL}^{a}	$f_{\text{hot}}^{\text{b}}$	ν_{line} (10^{14} Hz)	χ^2/dof
Continua	500	-0.29(6)	0.404(8)	0.37(2)	...	86/40
Absorption	...	-0.32(5)	0.424(9)	0.37(2)	2.91(3), 8.05(9)	58/36
Emission	1200(400)	0.4	0.26(6)	0.22(13)	3.9(5)	66/37

NOTE.—Numbers in parentheses indicate uncertainty in the final digit(s). Where no uncertainty is given, the value is very poorly defined ($< 1\sigma$).

^aPower-law ($F_\nu = N_{\text{PL}}\nu^{-\alpha_\nu}$) normalization at $\nu = 5 \times 10^{14}$ Hz, in μJy .

^bFlux density of the Rayleigh-Jeans power-law at $\nu = 2 \times 10^{15}$ Hz, in μJy .

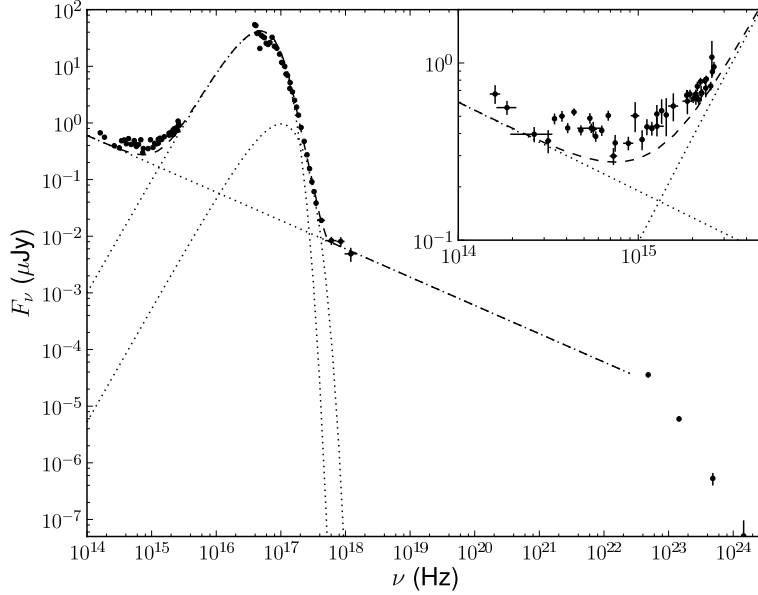


Fig. 6.— Multiwavelength spectrum of B0656, including the NIR-UV data, *Chandra* X-ray fluxed spectrum (this work) and γ -ray fluxes from the 2FGL catalog. We also sketch the fit to the X-ray spectrum by Zavlin & Pavlov (2004): two black-bodies with temperatures $T = 0.82, 1.72$ MK and a power-law with photon index $\Gamma = 1.5$. The X-ray absorbing column is $N_{\text{H}} = 1 \times 10^{20} \text{ cm}^{-2}$, and the optical/UV reddening $E(B - V) = 0.03$.

TABLE 8
PULSARS WITH IR-UV AND GeV DETECTIONS

Pulsar	d (kpc)	$\log \tau$	$\log B_0$	$\log B_{LC}$	$\log \dot{E}$	NIR	Optical	UV	$\log \eta$ X_{therm}	X_{PL}	γ -ray	E_{cut}	Γ_{MW}
Crab	2.0(5)	3.09	12.58	5.99	38.7	−5.3	−4.8	−4.2	...	−3.9	−3	5.8(5)	...
Vela	0.287(18)	4.05	12.53	4.65	36.8	−8.3	−7.9	−7.5	−4.6	−5.8	−2.0	3.2(1)	1.30
Geminga	0.25(9)	5.53	12.21	3.06	34.5	−7.0	−6.7	−5.7	−5.3	−4.3	−0.1	1.90(5)	1.20
B0656+14	0.29(3)	5.05	12.67	2.88	34.6	−6.6	−6.3	−5.6	−2.8	−4.8	−2.0	0.7(5)	1.50
B1055−52	0.35(15)	5.73	12.03	3.12	34.0	...	−6.3	−5.4	−3.4	−4.5	−0.85	1.3(1)	1.40
B1951+32	2.0(5)	5.03	11.69	4.87	36.6	...	−5	...	−4	−3.9	−1.7	4.5(1.2)	1.65
J0437−4715	0.156(1)	9.83	8.45	4.45	34.1	−5.8	−4.1	−4.8	−1.7	1.3(7)	1.55

NOTE.—All values in typical standard units, age τ in yr, magnetic field B in G, spin-down luminosity \dot{E} in erg/s, and high-energy cut-off E_{cut} in GeV. The efficiency η is the fraction of \dot{E} seen in each spectral window. For the efficiencies, we evaluate $\nu L_\nu/\dot{E}$ at 2×10^{14} , 5×10^{14} , 2×10^{15} , and 1×10^{18} Hz, for IR, Optical, UV, and X_{PL} respectively. For X_{therm} we calculate the efficiency using the bolometric luminosity of the hottest thermal component seen, and for the γ efficiency we use the 100 MeV–100 GeV integrated luminosities in Abdo et al. (2010b). The values of τ , B and \dot{E} have been corrected for the effect of proper motion, important for J0437−4715. Γ_{MW} is PL photon index that connects the IR, X-rays and γ -rays, with typical uncertainty around 0.05 (Figure 7).

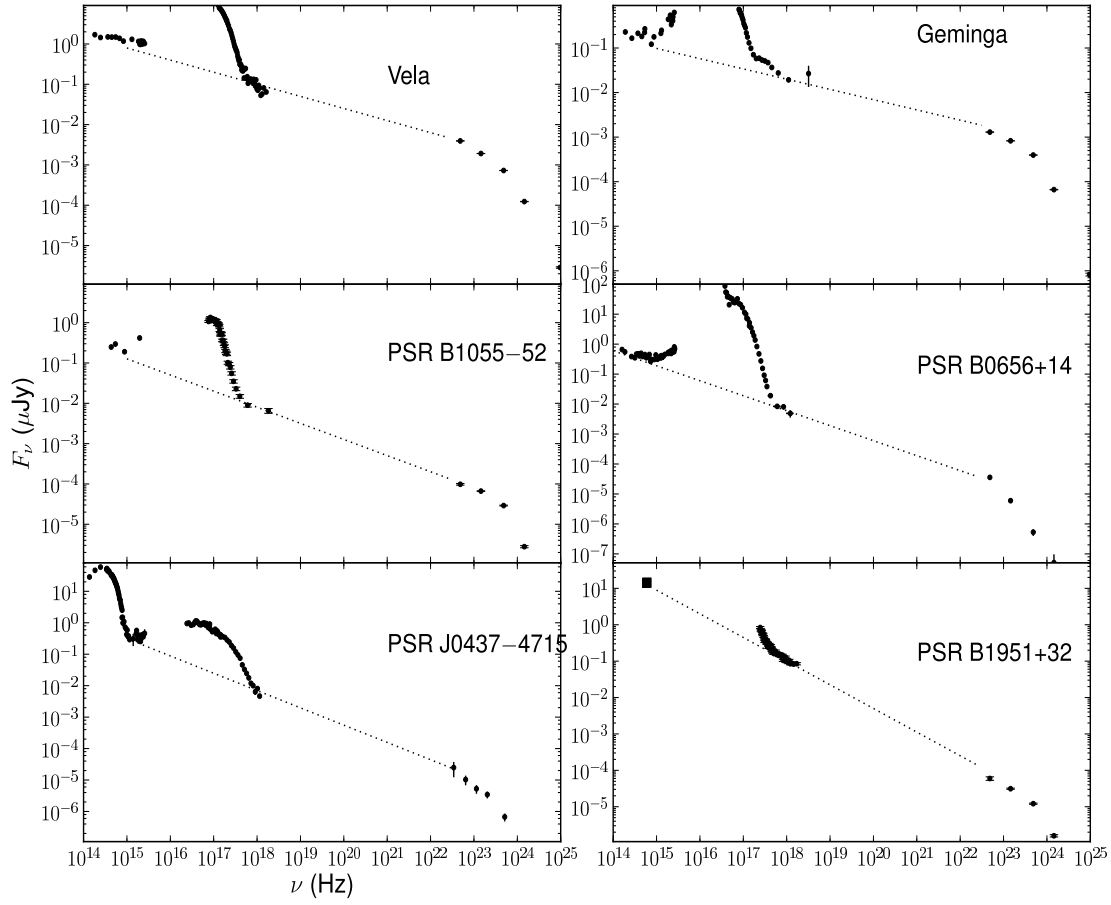


Fig. 7.— NIR/optical, X-ray and GeV spectra of pulsars detected in the NIR-UV window. Dotted lines are PLs drawn to connect the optical and γ -ray points (see text for discussion). Note that for J0437–4715, the lowest frequencies are dominated by its WD companion (see Durant et al. 2011).

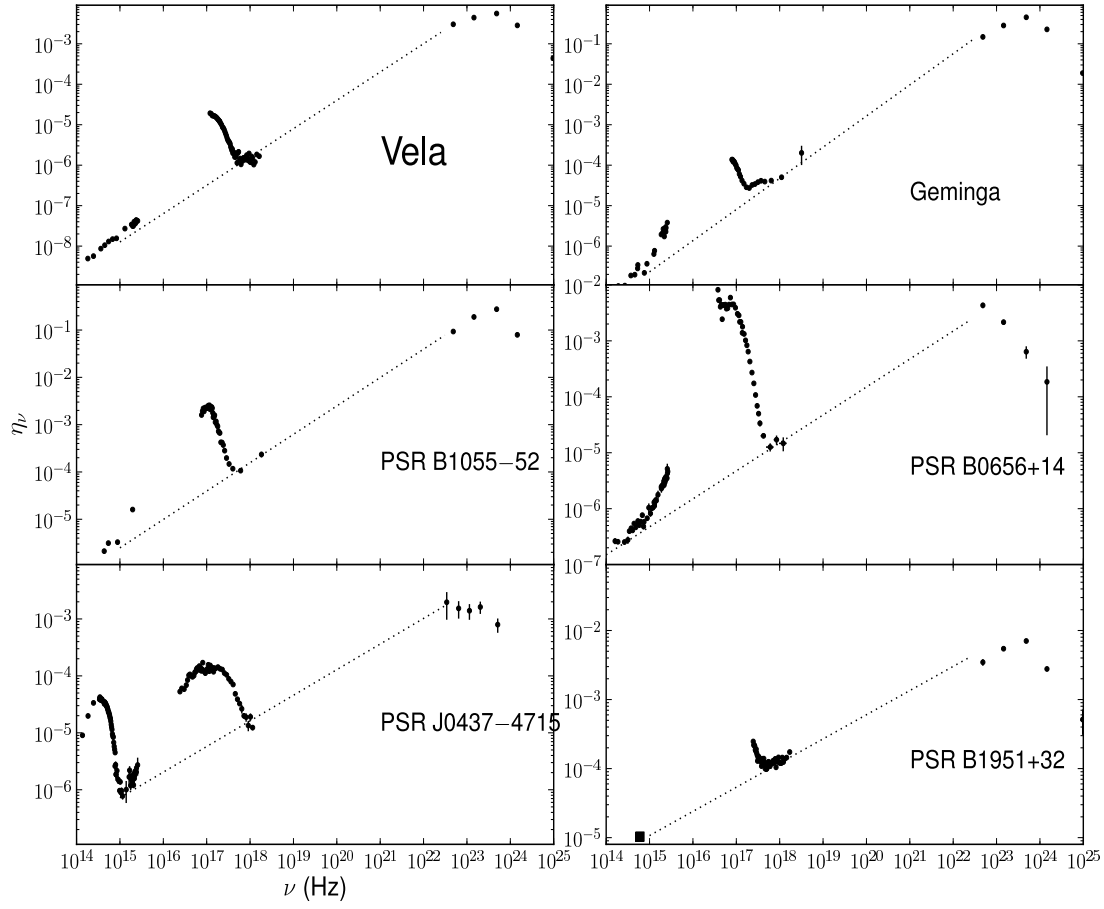


Fig. 8.— As Figure 7, but in terms of $\eta_\nu \equiv 4\pi d^2 \nu F_\nu / \dot{E}$

A. Data reduction details

A.1. STIS FUV grating

The source was imaged on the Far-Ultraviolet Multi Anode Micro-channel Array (FUV-MAMA). The low-resolution grating G140L (which covers the wavelength interval $\approx 1150\text{--}1700\text{ \AA}$) with the $52'' \times 0''.5$ slit was used. The data were taken during two consecutive orbits (including the target acquisition). The total scientific exposure time was 4950 s⁶. FUV-MAMA was operated in TIME-TAG mode, which allows the photon arrival times to be recorded with 125 μs resolution⁷.

For each exposure, we processed the raw “high-resolution” images (2048×2048 pixels; plate scale of $0''.0122$ per pixel — see §11 of the STIS IHB) using the most recent calibration files. As an output, we obtained flat-fielded low-resolution (1024×1024 pixels; plate scale $0''.0244\text{ pixel}^{-1}$; spectral resolution $0.58\text{ \AA pixel}^{-1}$) images and used them for the spectral analysis.

The processed images show a nonuniform detector background with a flat (constant) component and the so-called “thermal glow” component (Landsman et al. 1998) that dominates over most of the detector area and grows with increasing the temperature of the FUV-MAMA low-voltage power supply (LVPS) (the average LVPS temperatures were 42.60 and 42.84 C in the two consecutive orbits of our observation). The thermal glow is the strongest in the upper-left quadrant of the detector, where the dark count rate can exceed the nominal value, $6 \times 10^{-6}\text{ counts s}^{-1}\text{ pixel}^{-1}$, by a factor of 80. To reduce the contamination caused by the thermal glow background, the source was imaged close to the bottom edge of the detector.

We find the B0656’s spectrum centered at $Y = 102 \pm 2$ pixels in each of the flat-fielded images (the centroid position slightly varies with X), where X and Y are the image coordinates along the dispersion and spatial axes, respectively. Even at this location on the detector the background still exceeds the nominal value by a factor of 1.5–3 (typical values are $1\text{--}2 \times 10^{-5}\text{ counts s}^{-1}\text{ pixel}^{-1}$), depending on the position along the dispersion axis. To improve S/N, we co-added the exposures using the STSDAS task “mscombine” (the result is shown in Fig. 9). The Y -positions of the centroids differ by less than 3 pixels for different exposures and different wavelengths (X -positions).

To subtract the strong, nonuniform background, we used a custom IDL routine with capabilities of grouping and fitting the background and selecting an optimal extraction box size depending on the position along the dispersion axis (see also Kargaltsev et al. 2004). The background is taken from the two strips, $33 \leq Y \leq 92$ and $113 \leq Y \leq 172$, adjacent to the source region, $93 \leq Y \leq 112$. To obtain the spectrum with a sufficiently high S/N, we have to bin the spectrum heavily; after some experimenting, we chose 5 spectral

⁶The planned additional observations (6 orbits) were canceled because of the failure of STIS.

⁷However, the absolute time of photon arrival is not known to better than 1 s (Shibanov et al. 2005).

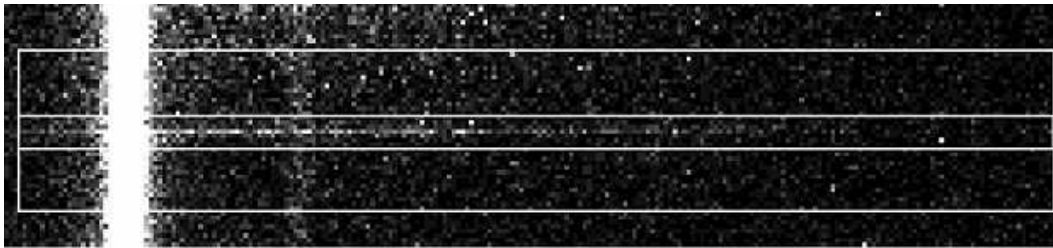


Fig. 9.— Raw FUV-MAMA spectrum of B0656. The boxes show approximate regions for the source and background extraction used in spectral analysis.

bins (λ -bins; see Table 3). The bins exclude the regions contaminated by the geocoronal emission (Ly α line and the OI line at 1304 Å). Since the OI line at 1356 Å is essentially not seen, we do not exclude the region around 1356 Å from the spectral analysis. The bins outside the contaminated regions were chosen to have comparable S/N (≈ 7 –11), whenever possible.

For each of the λ -bins, we calculate the total number of counts, N_t , within the extraction boxes of different heights (one-dimensional apertures): $A_s = 5, 7, 9, 7$, and 7 pixels, centered at $Y = 102$ for the first two λ -bins and at $Y = 103$ for the rest of the λ -bins. To evaluate the background, we first clean the background strips (see above) from outstanding ($> 10^{-3}$ cts s $^{-1}$ pixel $^{-1}$) values (“bad pixels”) by setting them to local average values. Then, for each of the λ -bins, we fit the Y -distribution of the background counts with a first-order polynomial (interpolating across the source region), estimate the number N_b of background counts within the source extraction aperture A_s , and evaluate the number of source counts, $N_s = N_t - N_b$ (Table 3).

The uncertainty δN_s of the source counts is evaluated as $\delta N_s = [N_s + \delta N_b^2(1 + A_s/A_b)]^{1/2}$, where δN_b is the Poisson background uncertainty scaled to the source aperture. We binned the distribution of background counts along the Y -axis with the bin sizes equal to A_s and calculated δN_b as the root-mean-square of the differences between the actual numbers of background counts in the bins and those obtained from the fit to the background. We calculated δN_s and S/N for various extraction box heights and found the A_s values maximizing S/N for each λ -bin (see Table 3).

We calculated the average spectral fluxes in the λ -bins:

$$\langle F_\lambda \rangle_i = \frac{\int_{\Delta\lambda_i} R_\lambda \lambda F_\lambda d\lambda}{\int_{\Delta\lambda_i} R_\lambda \lambda d\lambda} = \frac{C_i}{\int_{\Delta\lambda_i} R_\lambda \lambda d\lambda}, \quad (\text{A1})$$

where C_i is the source count rate in the i -th λ -bin corrected for the finite size of the source extraction aperture, and R_λ is the system response that includes the Optical Telescope Assembly throughput and accounts for the grating and slit losses and time-dependent sensitivity losses (Bohlin, 1999; see also §3.4.12 of the HST Data Handbook for STIS⁶ for details).

A.2. COS spectroscopy

B0656 was observed with the Cosmic Origins Spectrograph (COS) aboard *HST* with the G140L grism for a total of approximately 22 ks. With the 1105 Å central wavelength setting, the approximate sensitivity range is 1100–2250 Å, with resolution $R \approx 5000$ and cross-dispersion scale 0.023"/pix. We used the standard, clear primary science aperture (PSA), a 2".5 diameter circle. The FUV-A detector was operated in TIME-TAG mode, so that the arrival time (with precision of 32 ms) and pulse-height were recorded for each photon, together with its position. The pulse height is not a measure of the photon energy, but can nevertheless be used for screening some spurious events by excluding values 1–4 and 31⁸. The data were processed through the standard `calcos` pipeline, version 2.12, using the latest calibration files (January 2011) to produce corrected events lists (corrtag files). The raw 2-D image of the data is shown in Figure 10. Wavelength calibration spectra were taken during the observation, spatially offset from the source spectrum (Figure 10).

To extract fluxes from the data, we implemented an algorithm similar to the one used for STIS-FUV above. We converted corrected photon position to wavelength. Using the image in Figure 10, we found the source spectrum roughly along $y = 495$. Next, we split the data into bins of several columns each, we generated histograms of counts by y -coordinate in order to locate the source centroid and measured the width by fitting a Gaussian plus constant. This provided an estimate of the position and of the extent of the spectral trace in the cross-dispersion direction as a function of wavelength, as well as a measure of the background.

In each bin we summed the total number of counts falling within an extraction region, $\pm 1.7 \times \sigma_\lambda$ pix about the trace, where σ_λ is the width of the fitted Gaussian profile. The value of 1.7 was chosen by experimentation

⁶ http://www.stsci.edu/hst/stis/documents/handbooks/currentDHB/STIS_longdhtbTOC.html

⁸ [http://www.stsci.edu/hst/cos/documents/isrs/ISR2010_09\(v1\).pdf](http://www.stsci.edu/hst/cos/documents/isrs/ISR2010_09(v1).pdf)

to maximize the signal-to-noise. This aperture captures 91% of the incident light. The measured flux in the aperture is then

$$f_\lambda = \frac{N_\lambda - 2 \times 1.7\sigma_\lambda B_\lambda}{\sum_i R_{i,\lambda}} \quad (\text{A2})$$

where N_λ is the number of photons in the aperture, B_λ is the fitted background surface density, and $R_{i,\lambda}$ is the sensitivity function at position i in the dispersion direction within the bin. This flux was corrected to the standard calibration aperture (57 pix wide), and multiplied by a factor of 1.03 to account for the slightly diminished sensitivity of COS at the time of observation compared to the benchmark of the calibration (see ISR COS 2010-15⁹). We assume the uncertainty in the flux is dominated by Poissonian statistics in the source and background. Two regions of the spectrum could not be extracted due to strong geocoronal line contamination and the corresponding λ -bins were omitted.

A.3. STIS NUV prism

We also retrieved the data for the program GO-9156 from the *HST* archive. This program consisted of two visits during which PSR B0656+14 was observed with STIS NUV-MAMA. The first and second visits occurred on 2001 September 1 (start time 52,153.94 MJD) and 2001 November 16 (start time 52,229.47 MJD), respectively. The corresponding scientific exposure times were 6790.6 and 12761.0 seconds (3 and 5 orbits, respectively). In these observations $52'' \times 0''.5$ slit together with the PRISM (with central wavelength of 2125 Å, pixel scale $0''.024$) were used to obtain the dispersed spectrum of the target. NUV-MAMA was also operated in TIME-TAG mode.

For the spectral analysis we used flat-fielded low-resolution images (1024×1024 pixels) and reference files provided by the STIS pipeline. We find the B0656's spectrum centered at $Y = 499 \pm 2$ pixels in each of the flat-fielded images (the centroid position slightly varies along the dispersion axis X). To increase S/N we combined 5 exposures from the second (longer) visit using STSDAS `mscombine` task. The resulting image is shown in Figure 11. Most of the emission is confined between $X = 490$ and $X = 570$.

To extract the NUV spectrum, we use the procedure similar to that applied to the FUV data. We scan the count distribution within two strips, $430 \leq Y \leq 489$ and $510 \leq Y \leq 569$, adjacent to the source region, $490 \leq Y \leq 509$. The average background count rate at the source location is 1.2×10^{-3} counts s^{-1} pixel $^{-1}$, i.e., about two orders of magnitude higher than in the case of MAMA-FUV observation. Therefore, to obtain the spectrum with a sufficiently high S/N, we bin the spectrum into 8 spectral bins with $S/N \approx 5\text{--}11$.

Contrary to grating observations, the conversion from the pixel number (along the dispersion axis) to wavelength is nonlinear for PRISM spectra¹⁰. Since the PRISM dispersion depends strongly on the wavelength (the resolution decreases with increasing wavelength¹¹), even a small shift (in terms of pixels) will translate into a large shift in terms of the assigned wavelength at longer wavelengths ($\lambda \gtrsim 3000$ Å). Furthermore, because of the strong dependence of the PRISM throughput on wavelength, assigning a slightly incorrect wavelength can result in a large error in the derived flux at $\lambda \gtrsim 3000$ Å. Hence, it is important to accurately determine the wavelength zeropoint. The latter depends on the actual position with respect to the aperture (slit) center as well as on the offsets caused by the Mode Selection Mechanism (MSM) (positioning/tilt of the slit/PRISM) non-repeatability and thermal drift.

The *wavecal* exposures taken between the science exposures are expected to accurately account for the last two effects while the source position within the slit can be measured from the CCD images taken during each visit through the same $52'' \times 0.5''$ slit aperture. Although at the first glance the source appears to be well centered within the aperture, a more detailed investigation revealed a $0''.045 \pm 0''.02$ shift (about 9% of the slit

⁹[http://www.stsci.edu/hst/cos/documents/isrs/ISR2010_15\(v1\).pdf](http://www.stsci.edu/hst/cos/documents/isrs/ISR2010_15(v1).pdf)

¹⁰See §12.1 of the STIS Instrument Handbook for details

¹¹See §4.4 of the STIS IHB (http://www.stsci.edu/hst/stis/documents/handbooks/currentIHB/c04_spectros5.html#310764)

width) of the position of the best-fit source centroid with respect to the slit center. This relatively small shift amounts to 1.6 MAMA-NUV pixels. Such a difference in assigning the MAMA-NUV wavelength zeropoint would produce a noticeable difference in the flux at $\lambda \gtrsim 2600 \text{ \AA}$ because the throughput curve is steep and the resolution very low for these wavelengths. Hence we account for this shift when assigning the wavelength zeropoint. Since the measured shift has a large associated uncertainty, we choose to ignore the spectrum at $\lambda > 2950 \text{ \AA}$ (at these wavelengths the $0''.02$ uncertainty may have a large impact on the flux calibration). Additionally, the steep throughput curve and low dispersion (compared with the line-spread function) mean that the apparent flux at wavelengths $\lambda > 3000 \text{ \AA}$ would be contaminated by shorter wavelengths. This effect is difficult to account for, giving another reason to consider the flux calibration unreliable for $\lambda > 2950 \text{ \AA}$ and limit the extraction of the NUV spectrum to the $1790 - 2950 \text{ \AA}$ range.

Aside from the caveats above, we use the same flux calibration procedure as for the STIS FUV data to derive the NUV spectrum.

A.4. ACS/WFC Ramp Filter Photometry

The Advanced Camera for Surveys (ACS) aboard *HST* provides three ramp filters for narrow-band imaging. A ramp filter has a band-pass which depends on the part of the filter that light passes through, hence one can choose from a range of central wavelengths, with about 10% bandwidth in each case. We utilized each of the three ramp filters, for a total of 11 photometric points, see Table 1. The pipeline-produced, drizzle-combined images are shown in Figure 12.

We use the same aperture size for all filters and central wavelength settings, because the width of the PSF varies only slightly with wavelength ($\sim 15\%$ across the optical range). We used $r = 0''.125$ (2.5 pixels), which is close to the typical FWHM, and gives nearly optimal SNR in all the images. The encircled energy fraction within the aperture varies from 52% in the red to 70% in the blue. The background was taken from an annulus with the same center and radius $1'' < r < 1''.75$. To estimate the aperture correction, we measured the flux within $r = 0''.125$ and $0''.5$ (the standard calibration aperture), for the nearby brighter star N7, located approximately $10''$ northwest of B0656 (Koptsevich et al. 2001). This is one of the few field sources that has a point-source profile (most field sources are extended, i.e., galaxies), and photometry shows that it is indeed a star (see Section A.6). Since the filter band-pass is position-dependent, it is necessary to choose a calibration source for the aperture correction as close to the source of interest as possible. Finally, the fluxes were calculated using the photometric zero point delivered by the pipeline¹².

The CTE correction was implemented following the prescription of Chiaberge et al. (2009)¹³. We interpolated between the August 2005 and March 2006 values to find the parameters appropriate to our epoch of observation, giving a mean correction $\delta\text{mag} = 10^a \times \text{SKY}^b \times \text{FLUX}^c \times (Y_{\text{tran}}/2000) = 0.04 \text{ mag}$, where $a = 0.40$, $b = -0.26$, $c = -0.47$, and the number of transfers in the y direction during readout was $Y_{\text{tran}} \approx 1100$ for 4049, 4401, 4780, 5165, 7956, 8751, 9491 \AA and $Y_{\text{tran}} \approx 990$ for 5566, 6244, 6822, 7393 \AA .

A.5. NICMOS photometry

We downloaded the NICMOS data and the best available calibration files from the archive. Each image is a 636.1s exposure in ACCUM mode. This mode is *non-standard*: there are multiple reads at the end of the exposure rather than reads at regular intervals throughout the exposure. This leads to inefficient screening of CRs. Four images per orbit were obtained using a dither pattern, with one orbit for F110W (2554s total integrations), two for F160W (5089s total integration) and three for F187W (7633s total integration - see Table 1).

We processed the data, utilizing the custom-made dark file provided by STScI at our request. This was required due to the time-variability of the detector temperature both with the age of the instrument and

¹²www.stsci.edu/hst/acs/documents/isrs/isr0711.pdf

¹³<http://www.stsci.edu/hst/acs/documents/isrs/isr0901.pdf>

time elapsed since its previous power-on. The processing of the raw data into final images shown in Figure 13 included the following steps:

- the pedestal correction removes bias-like additive signal from each amplifier quadrant by calculating the median pixel values, after rejection of stars and hot pixels;
- the task `multidrizzle` resamples images to a common reference frame, removing geometric distortion. It also compares the median of these images with the input resampled images, in order to identify and reject some cosmic rays/bad pixels;
- final images were made by a median combination. We found that the median gave better result than the average, since the ACCUM mode results in a very high incidence of cosmic rays.

Photometry was performed using small apertures of $r = 2.5 \text{ pix}$ ($0''.19$), with the aperture correction to the $0''.5$ nominal aperture calculated from the photometry of Star N7. The dither pattern sometimes took N7 close to the chip edge, so we used only those frames in which N7 was sufficiently far from the edge to avoid low sensitivity pixels in the $0''.5$ aperture. The calibrated zero point is defined relative to 1.15 times the flux in the $0''.5$ aperture (equivalent to correcting to the “infinite aperture”). The final flux was calculated using the header PHOTFNU keyword, provided by the pipeline.

A.6. Optical-IR calibration check

In an effort to check the calibration of our observations, we consider the flux measurements of field star N7 (see Figure 14), also known as 2MASS J06594760+1414253, in the nominal-size aperture $0''.5$. Using broad-band photometry (*HST* in the optical and 2MASS in the NIR) to estimate the spectral class and reddening of the source¹⁴, we find that the star spectrum approximately matches a 4000 K (K-type) giant at 2.5 kpc (i.e., the Perseus Arm) reddened by $E(B - V) = 0.35$ (the photometry also matches a dwarf at $\sim 80 \text{ pc}$, but the reddening is unreasonably high for such a small distance). The broad-band fluxes and the fluxes we derive appear to match very well in the optical.

Our IR fluxes for N7 are about 10% higher than those of Koptsevich et al. (2001). The likely reason for the discrepancy is that these authors also used the exposures of N7 which fell onto the low-sensitivity edges of the detector. Our IR fluxes are, however, about 20% lower than the 2MASS fluxes. The 2MASS extraction aperture includes the fluxes of three faint nearby sources (resolved by *HST*), which contribute roughly 10% to the NIR flux each, and give summed fluxes consistent with the 2MASS ones, within the uncertainties.

¹⁴See our star type fitting tool at <http://www.astro.ufl.edu/~martin.durant/Sclass.html>

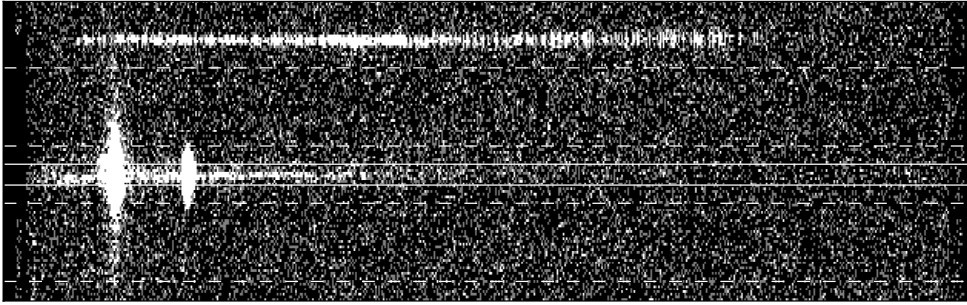


Fig. 10.— COS image of PSR B0656+14, showing events filtered by pulse height and data quality (binning for display purposes is 5×2 original pixels, $0''.115 \times 0''.184$). Approximate spectral and sky extraction regions are shown (see text). The bright strip across the top of the image is the calibration spectrum, and the two prominent bright patches are images of the round aperture centered on bright geocoronal emission lines, which look elliptical after binning.

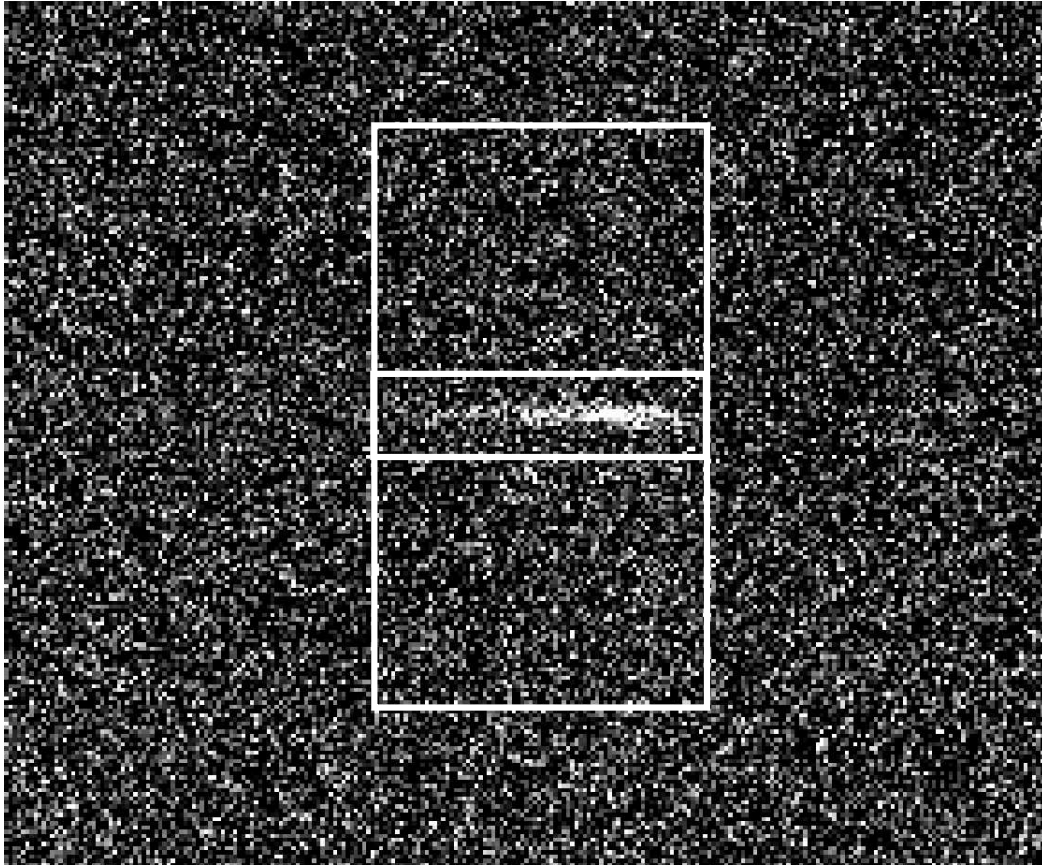


Fig. 11.— Raw NUV-MAMA spectrum of B0656. The boxes show approximate regions for the source and background extraction used in spectral analysis.

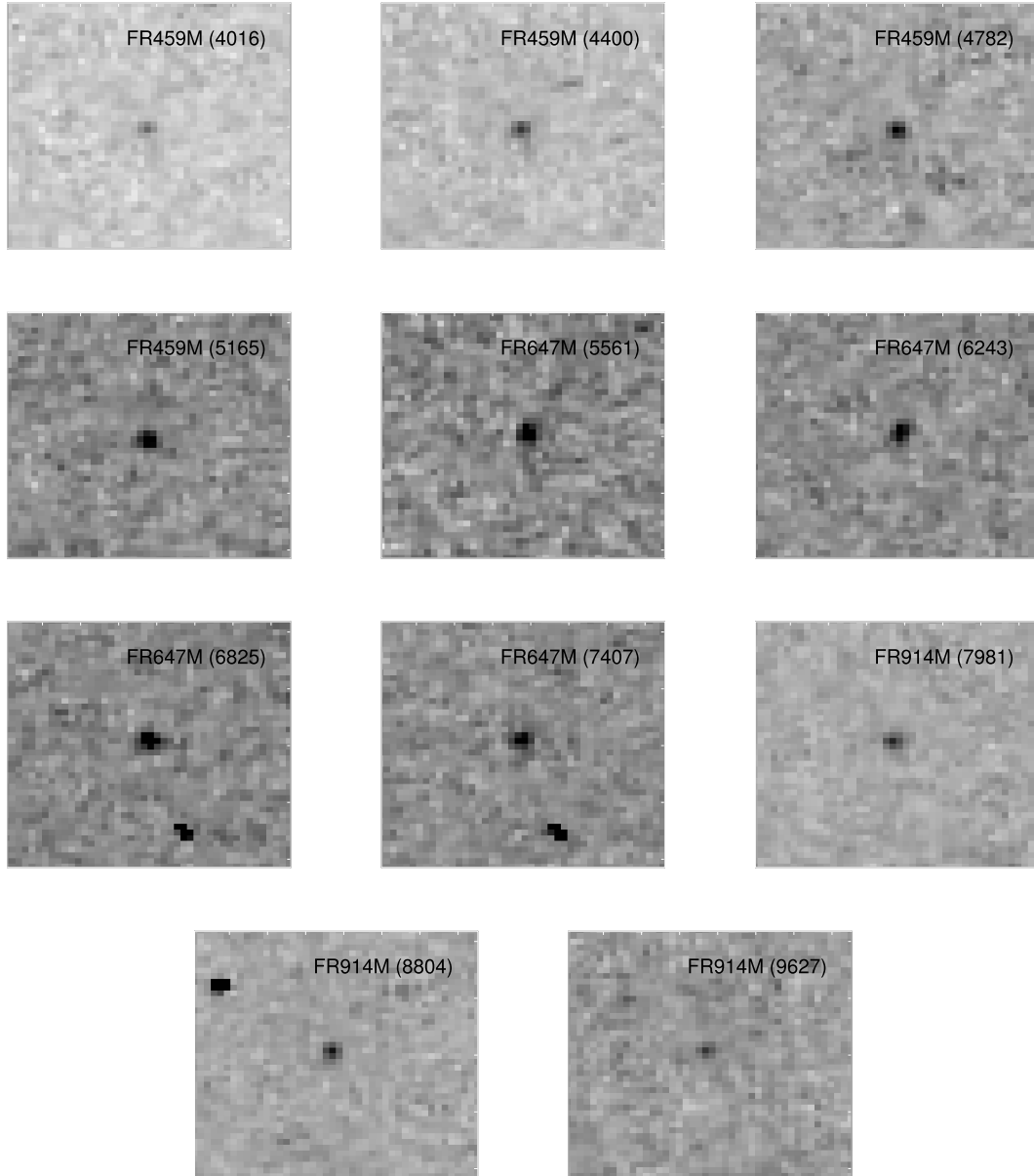


Fig. 12.— ACS/WFC ramp filter imaging of PSR B0656+14. North is up, and images are $2.2'' \times 2.2''$

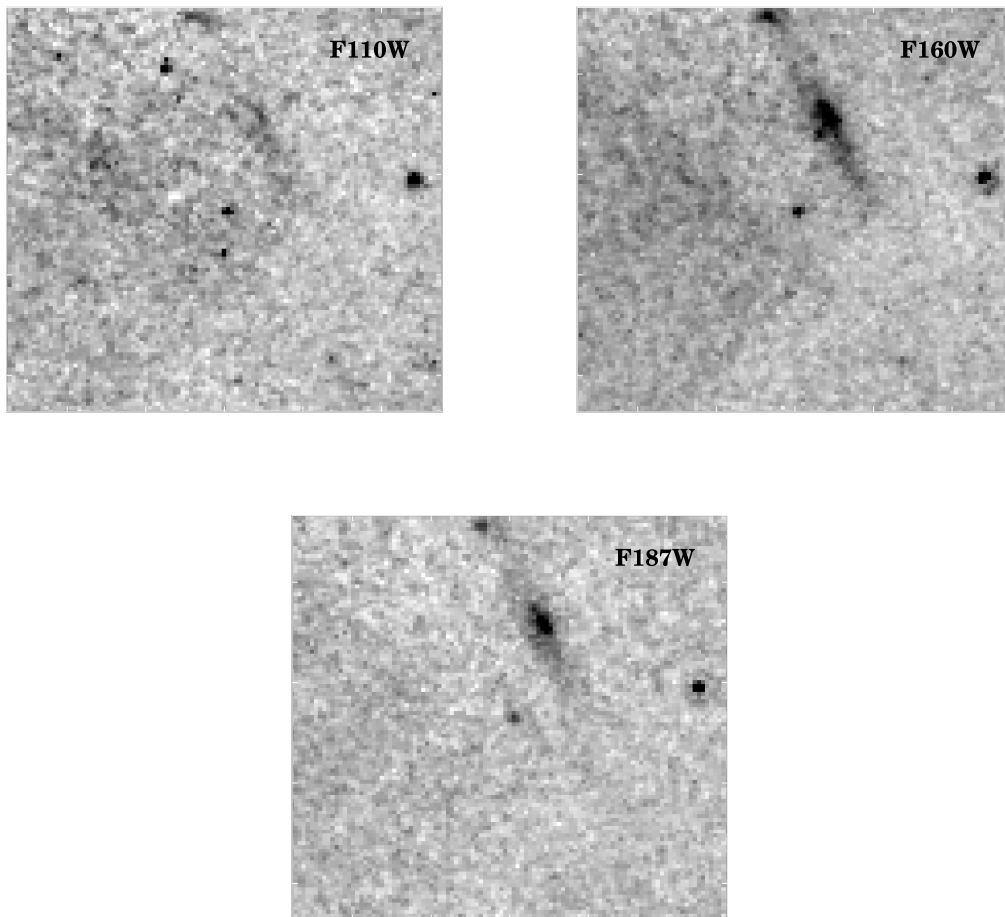


Fig. 13.— NICMOS images of B0656. Field is centered on the pulsar, and $4''$ on each side. Compare to the images in Figure 3 of Koptsevich et al. (2001).

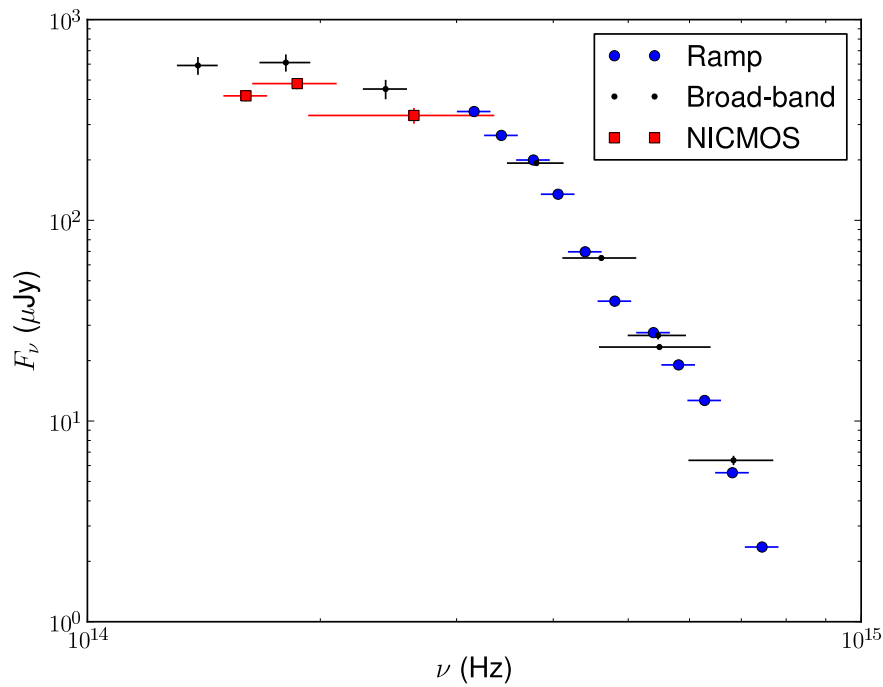


Fig. 14.— Optical-IR spectrum of field star N7, showing 2MASS and HST broad-band photometry (black points), NICMOS photometry (red squares) and ACS narrow-band photometry (blue circles). Statistical uncertainties are quite small in most bins, and hence not seen.